# Flow field and heat transfer investigation in tubes of heat exchangers with motionless scrapers

J.P. Solano[a,*], A. García[a], P.G. Vicente[b], A. Viedma[a]

[a] *Universidad Politécnica de Cartagena, Departamento de Ingeniería Térmica y de Fluidos, Campus Muralla del Mar, 30202 Cartagena, Spain*
[b] *Universidad Miguel Hernández, Departamento de Ingeniería de Sistemas Industriales, Avenida de la Universidad, 03202 Elche, Spain*

**Abstract**

Flow pattern and thermal-hydraulic characteristics in an innovative tube insert have been experimentally and numerically investigated. The insert device is a concept envisioned for reciprocating scraped surface heat exchangers. It consists of a concentric rod, that mounts an array of semicircular plugs fitted to the inner tube wall. In motionless conditions, the insert works as a turbulence promoter, enhancing heat transfer in laminar regime. Fundamental flow features in the symmetry plane of the tube have been assessed with Particle Image Velocimetry technique. A general model of the flow mechanism has been defined, identifying three regions along a geometrical pitch: recirculation bubbles, flow acceleration and transverse vortex. Results have been complemented with experimental data on pressure drop and heat transfer. The transition onset is clearly identified, and the mechanisms that promote turbulence at low Reynolds number are investigated and discussed. CFD simulations for different Reynolds numbers provide a further insight into the relation of the flow structures with wall shear stress, and their role on the local heat transfer augmentation.

*Corresponding autor
*Email address:* `juanp.solano@upct.es` (J.P. Solano)

*Keywords:* tube inserts, flow pattern, heat transfer enhancement, friction factor

## Nomenclature

| | |
|---|---|
| $A$ | annuli cross sectional area (m) |
| $D$ | tube inner diameter (m) |
| $D_h$ | hydraulic diameter (m) |
| $d$ | rod diameter (m) |
| $F$ | fluid force (N) |
| $h$ | heat transfer coefficient (W m$^{-2}$ K$^{-1}$) |
| $k$ | thermal conductivity (W m$^{-1}$ K$^{-1}$) |
| $\dot{m}$ | mass flow rate (kg s$^{-1}$) |
| $P$ | pitch of the insert devices (m) |
| $\Delta\, p$ | pressure drop across the test section (Pa) |
| $Q$ | overall electrical power added (W) |
| $Q_\ell$ | heat losses in the test section (W) |
| $q$" | heat flux (W m$^{-2}$) |
| $R3$ | performance factor [-] |
| $T$ | temperature (°C) |
| $t$ | plug thickness (m) |
| $v_f$ | mean fluid velocity (m s$^{-1}$) |

*Dimensionless groups*

| | |
|---|---|
| $f_h$ | Fanning friction factor, $\Delta p D_h / 2\rho {v_f}^2 L$ |
| $\mathrm{Nu}_h$ | Nusselt number, $h D_h / k$ |
| Pr | Prandtl number, $\mu c_p / k$ |
| $\mathrm{Re}_h$ | Reynolds number, $\rho v_f D_h / \mu$ |

| | |
|---|---|
| $c_F$ | force coefficient, $F/\frac{1}{2}\rho {v_f}^2 A$ |
| $C_f$ | skin friction coefficient, $\tau_w/\frac{1}{2}\rho {v_f}^2$ |

*Greek symbols*

| | |
|---|---|
| $\mu$ | dynamic viscosity (kg m$^{-1}$ s$^{-1}$) |
| $\rho$ | fluid density (kg m$^{-3}$) |

*Subscripts*

| | |
|---|---|
| $a$ | augmented tube |
| $b$ | based on bulk temperature |
| $h$ | based on hydraulic diameter |
| $in$ | tube inlet |
| $out$ | tube outlet |
| $s$ | smooth tube |

## 1. Introduction

Heat transfer processes in the food, chemical and pharmaceutical industries frequently deal with highly viscous products. The performance of heat exchangers working under these conditions is usually bad, as a result of the encountered laminar regime [1]. Moreover, the heat transfer surfaces may become coated with a deposit of solid material after a period of operation. This phenomenon, known as fouling, causes a reduced overall heat transfer coefficient [2]. Heat exchangers are generally overdesigned to compensate for the anticipated fouling. In addition, cleaning operations decrease equipment availability, which causes as well a considerable economic impact [3].

Among the several techniques commercially available for tube-side heat transfer enhancement, insert devices play an important role in laminar flow, where the dominant thermal resistance is not limited to a thin boundary layer adjacent to the flow. Devices that mix the gross flow are of primary interest for these applications, though the associated pressure drop penalty strongly influences their economical feasibility. Several works have reported on the thermal-hydraulic characteristics of twisted tapes in laminar flow [4, 5]. Static mixers [6] and displaced elements [7] have also been considered as suitables devices for tube-side enhancement through early turbulence promotion. Wire meshes constitute as well a successful solution for laminar tube-side enhancement [8, 9], yielding to equipment size reduction and energy savings. Recently, flow pattern and thermal-hydraulic characteristics of novel tube insert geometries have been reported. Special interest for the present work is focused on rod-based devices, like helical-screw inserts [10, 11] and baffle-type tube inserts [12, 13].

Fouling mitigation in inserted tubes is an important issue. Some experimental works have proved the beneficial effect of insert devices (e.g. wire matrix turbulators) on the reduction of the fouling rate [14]. Self-vibrating wire coil inserts also mean a successful solution for simultaneous heat transfer enhancement and fouling mitigation [15].

In the present work, an innovative tube insert is presented. Within the tube there is a concentric rod, mounting an array of semi-circular elements with a pitch P=5D (see Fig. 1). These elements fit the internal diameter of the tube. The arrangement of the insert device increases the global fluid velocity, and the blockage imposed by the elements promotes continuous mixing of core regions with peripheral flow. As a result, high tube-side heat transfer coefficients can be achieved within laminar flows. In applications with severe fouling tendency, the inserts can be connected to an hydraulic piston, providing them with self-cleaning reciprocating motion.

The main objective of this work is to assess the fundamental flow features and thermal-hydraulic characteristics in tubes of these kind of heat exchangers, when they work in motionless conditions. This mode of operation occurs in applications where the device is only activated sporadically, for fouling mitigation. Besides, the thorough analysis of the motionless scraper extends the knowledge on the physical mechanisms of laminar heat transfer enhancement through gross flow mixing.

Particle Image Velocimetry (PIV) technique is employed for obtaining the two-dimensional velocity field in the symmetry plane of the tube in laminar regime. The main flow features occurring in the tube are identified, and the influence of Reynolds number in the macroscopic flow structures is clearly assessed. Experimental results of Fanning friction factor for a wide range of Reynolds numbers are contrasted with the visualization data, allowing to identify the onset of transition at low Reynolds number, and its influence on the flow behavior. Heat transfer results are also presented, and an evaluation of the thermal-hydraulic performance of the insert device is assessed. The contribution of the flow structures to the local shear stress and heat transfer characteristics is analyzed with the numerical simulation tool Fluent, complementing the experimental data and providing further information towards the holistic understanding of the physical flow nature.

## 2. Experimental program

### *2.1. Visualization Facility*

The facility depicted in Fig. 2 was built in order to study the flow pattern induced by a wide variety of insert devices in round tubes [16]. The main section consists of a 32 mm diameter acrylic tube installed between two reservoir tanks, that stabilize the flow. The flow temperature is regulated by an electric heater and a thermostat placed in the upper reservoir tank. The flow is impelled from the lower calm deposit to the upper one by a gear pump, which is adjusted by a frequency converter. By using mixtures of water and propylene-glycol at temperatures from 20°C to 60°C, Reynolds numbers between 100 and 20 000 can be obtained. The tests presented in this work were carried out employing a mixture of 90% propylene-glycol and 10% water, at temperatures from 25°C to 50°C, yielding Reynolds numbers in the range from 30 to 300. The strong deviation and acceleration induced by the insert device (see Fig. 1) prevented the appearance of substantial buoyancy forces, eventually induced by heat losses.

The test section was placed downstream five scraper pitches (25D), thus ensuring periodic flow conditions. To improve optical access in this section, a flat-sided acrylic box was placed around. The box was filled with the same test fluid that flows through the test section. Particle Image Velocimetry (PIV) has been employed for flow visualization.

PIV is a well-known technique to obtain global velocity information , instantaneously and with high accuracy [17]. In these experiments, planar slices of the flow field containing the symmetry plane of the inserted device were illuminated. The flow was seeded with polyamide particles of 57 $\mu$m mean diameter. The camera viewed the illuminated plane from an orthogonal direction and recorded particle images at two successive instants in time in order to extract the velocity over the planar two-dimensional domain. 2D velocity fields along a scraper pitch were assembled to provide an overall insight of the flow structure.

The spatial resolution of the measurement is 110 $\mu$m/pixel. A 1 mm thick light sheet is created by a pulsating diode laser of 808 nm wavelength. A computer synchronizes the camera shutter opening and the laser shot at sampling frequencies between 250 and 500 Hz, most appropriate for the test conditions.

Image processing was carried out with the software 'vidPIV', that applies a cross-correlation algorithm between consecutive images. The interrogation window size used for PIV processing was $32 \times 32$ pixels, with a 50% overlap. Subsequent adaptive cross-correlation algorithm [18] was applied with an interrogation window size of $16 \times 16$ pixels and 50% overlap. To obtain a clear velocity field, after the images were correlated, a global and a local filter were applied to remove outliers. The resulting vectors were averaged over fifty realizations. Using the standard formula for 20-to-1 odds, $\pm 1.96\, \sigma\, N^{-0.5}$, the uncertainty in PIV measurements is about 3%. Taking into account the uncertainty in the computation of pixels displacements, the final uncertainty in PIV measurements rises to 5%.

### *2.2. Thermal-hydraulic tests*

A schematic diagram of the set-up for thermal-hydraulic tests is shown in Fig. 3. The test section consists of a 4 m long stainless steel tube where the scraper is inserted. The inner and outer diameters of the tube are 18 mm and 20 mm. Propylene-glycol is continuously impelled from an open reservoir tank towards the test section by a variable-speed gear pump. A secondary circuit is used for regulating the working fluid temperature. Mass flow rate is measured by a Coriolis flowmeter. All the instrumentation installed on the main circuit is connected to a HP 34970A Data Acquisition Unit.

Heat transfer experiments were carried out under uniform heat flux (UHF) conditions, through Joule effect tube heating. Power was supplied by a 6 kVA transformer connected to the tube with copper electrodes. A variable auto-transformer in series with the main transformer was used for power regulation. The heat transfer test section was defined by the length between electrodes, $l_h$=55D. Six axial positions for wall temperature measurement were consecutively placed starting from a distance

30D downstream the first electrode, covering equally spaced sections over an insert pitch. The loop was insulated by an elastomeric thermal insulation material of 20 mm thickness and thermal conductivity 0.04 W/(m K) to minimize heat losses. The overall electrical power added to the heating section, Q, was calculated by measuring the voltage between electrodes (0-15 V) and the electrical current (0-600 A).

Fluid inlet and outlet temperatures $T_{in}$ and $T_{out}$ were measured by submerged type RTDs (Resistance Temperature Detectors). Since the heat was added uniformly along the tube length, the bulk temperature of the fluid at each measuring section, $T_b\left(x_{p,j}\right)$, was calculated by considering a linear variation with the axial direction. Average outside surface temperature of the wall $\overline{T}_{wo,j}$ at each section was computed by averaging the temperatures measured by six thin film thermocouples type$-$T peripherally spaced every 60$^{\text{o}}$. Two calibration tests with no electrical heating were performed: the first test was carried out to determine heat losses in the test section $Q_\ell$ by measuring $(T_{in} - T_{out})$ at low flow rates, and the second test at high flow rates (where $T_{in} \approx T_{out} \approx \overline{T}_{wo}$) to calculate the lay-out resistances of the thin film thermocouples. Further details of the calibration tests are given in Vicente et al. [19].

Heat flux added to the test fluid $q$" was calculated by subtracting heat losses to the overall electrical power added in the test section. The inner wall temperature $\overline{T}_{wi,j}$ for each experimental point was determined by using a numerical model that solves the steady-state one-dimensional radial heat conduction equation in the tube wall from the following input data: $\overline{T}_{wo,j}$, $Q$, $Q_\ell$, and $T_b\left(x_{p,j}\right)$. The local Nusselt number was calculated by means of

$$Nu_{h,j} = \frac{D_h}{k}\frac{q"}{\overline{T}_{wi,j} - T_b\left(x_{p,j}\right)} \tag{1}$$

Nusselt numbers calculated with Eq. (1) were corrected by the factor $\left(\mu_{wi}/\mu_b\right)^{0.14}$

(Shah and London [20]) to obtain correlations free from variable properties effects. Ensembled averages over the six sections were computed to account for the mean Nusselt number over the scraper pitch.

Pressure drop tests were carried out under isothermal conditions. The test section length, $l_p$=100D, was preceded by a development region of $l_e$=30D length, in order to establish periodic flow conditions. The hydraulic diameter of the annular section, $D_h = D - d$, was used as the reference dimension to calculate the friction factor. Fanning coefficients $f_h$ were determined from fluid mass flow rate and pressure drop measurements as

$$f_h = \frac{\Delta p}{l_p} \frac{\rho \pi^2 \left(D+d\right)^2 D_h^3}{32 \dot{m}^2} \tag{2}$$

A highly accurate differential pressure transducer was employed to measure pressure drop $\Delta p$ along the test section. Four pressure holes separated by 90° were coupled to each end of the pressure test section.

Experimental uncertainty was calculated by following the "Guide to the expression of uncertainty in measurement" published by ISO [21]. Uncertainty calculations based on a 95 percent confidence level showed maximum values of 4% for Reynolds number, 3.5% for Prandtl number, 9% for Nusselt number and 3% for friction factor.

## 3. Numerical program

The geometry of the computational model was created using the software Gambit. It consists of the fluid volume of the inserted tube, thus being an annular duct to which semi-circular plugs where substracted every $P/2$ distance. In order to solve the conjugate heat transfer problem between the fluid, the tube and the insert [22], the plugs and the solid tube were also included in the computational grid.

The scraper extends over seven pitches, being the flow solution in the fifth one subjected to analysis. This ensured periodic flow conditions in the entrance and flow free of outlet effects. The geometrical symmetry of the problem proved to ensure also flow symmetry for the range of Reynolds number under study. Thus, only half domain was modelled.

Structured, hexahedral mesh was employed. A double compression ratio was introduced in both sides of the plugs, where greater variations of the flow pattern were expected due to the geometry constriction, and in radial direction, to ensure better solution where higher velocity gradients where expected. The finite volume FLUENT code (commercially available software, version 6.3) was employed for the solution of the continuity, momentum pressure-based and energy equations. Full Navier-Stokes equations were treated in general, body fitted coordinates. Control-volume storage scheme was employed where all variables were stored at the cell center. Second order upwind scheme was used in order to interpolate the face values of computed variables. Implicit segregated solver solved the governing equations sequentially. In this study pressure-velocity coupling algorithm SIMPLE was used.

Two sets of simulations were performed: isothermal computations, for the solution of the shearing profiles, and heat transfer simulations. Internal heat generation in the stainless steel tube was implemented as boundary condition, thus reproducing the conditions of the experimental tests. Nylon was employed as material of the plugs. Temperature-dependent properties were considered for the propylene-glycol, following the same correlations employed in the experimental data reduction program.

## 4. Flow pattern assessment

### 4.1. Main flow characteristics

Fig. 4 (left) depicts the velocity field in the symmetry plane of the scraper, divided by the mean flow velocity $\vec{v}/v_{med}$, for Reynolds number $\mathrm{Re}_h = 213$. A horizontal plane containing the tube axis also divides the visualization field into bottom and top sections, with odd-symmetry characteristics.

Following the sequence of the flow direction (left to right), a region of low velocity is found in the top section, downstream the first plug. The flow vectors enclosed to the picture move backwards, which is associated to flow separation and recirculation. Afterwards, a high velocity region grows along the streamwise direction. This stream impacts against the front side of the third plug, generating a transverse vortex.

The reversed assembly of the even plugs provides the flow with the aforementioned odd-symmetry characteristics: the structures occurring in the top section, between the first and second plug, are repeated in the bottom section, between the second and third plug. This condition can be read as follows:

$$v_z\left(z + P/2, r\right) = v_z\left(z, r\right) \tag{3}$$

$$v_r\left(z + P/2, r\right) = -v_r\left(z, r\right) \tag{4}$$

$$v_\theta\left(z, r\right) = 0 \tag{5}$$

In order to clarify the flow structure, a simple model of the flow mechanism is elaborated, supported by the direct observation of the three-dimensional flow features in the visualization facility. The flow trajectory and the resulting structures are outlined in Fig. 4 (right):

The mean flow generated by the global pressure gradient presents a meandering path: the presence of the plugs every $P/2$ distance forces the flow to sharply turn and move towards the section not affected by the blockage. The resulting deviation induces a local velocity increase, as the flow area is approximately reduced by one half. The main stream reattaches to the wall and proceeds towards the tube. As this stream expands to the annular section, two counter-rotating recirculation bubbles are created behind the plugs. These bubbles converge in the symmetry plane, where the local structure with low velocity, reversed flow vectors is visualized. The reattached flow finally impacts against the next plug, creating a transverse vortex rolling over a curved axis parallel to the front side of the plug.

### *4.2. PIV results*

The analysis of the flow structure at different Reynolds numbers is of primary importance to understand the physical mechanisms that promote early transition to turbulence, heat transfer enhancement and pressure losses.
To account for this analysis, PIV results for the working range $36 \leq \mathrm{Re}_h \leq 265$ are presented in Fig. 5. A fair estimation of the global fluid-dynamic phenomena existing in the tube is provided by these 2D footprints. Three main aspects of the flow features that strongly depend on Reynolds number are next stated: the length of the recirculation bubbles, the growth of the transverse vortex and the axial velocity profile in the region of flow acceleration.

#### *4.2.1. Local structures: recirculation bubbles and transverse vortex*

The kinematic behaviour of the recirculation bubbles is outlined in the vectorial picture of Fig. 4 (left). The position where the flow reverses is characterized by a strong downward component. However, local velocity values in the reversed flow section are substantially lower than the mean flow velocity: for the range of Reynolds number $36 \leq \mathrm{Re}_h \leq 150$, these values are of the order $v/v_{med} \approx 0.1$.

The characteristic length of the bubbles, L, is defined as the distance between the rear part of the plug and the average axial location where the flow in the symmetry plane reverses. The evolution of this length for increasing Reynolds numbers can be observed across Fig. 5, showing a rapid growth up to $\mathrm{Re}_h \approx 150$.

Fig. 6 shows a detailed representation of this phenomenon, where the characteristic bubble length is non dimensionalized with the scraper pitch, L/P. This evolution quantifies the tendency previously stated, depicting the growth of the bubbles towards an asymptotic value of the order of L/P$\approx 0.3$.

The evolution of the transverse vortex that appears in the front side of the plugs can also be analyzed. For $\mathrm{Re}_h < 60$, instead of a vortex appearance, the stream decelerates towards a stagnation region. For the range $60 < \mathrm{Re}_h < 200$, local velocities in the vortex and in the periphery increase with Reynolds number, and the size of the vortex increases substantially.

For higher Reynolds numbers, the vortex size diminishes and the peripheral velocities increase. This phenomenon is associated to the growth of the recirculation bubbles up to its asymptotic value, and the appearance of low-Reynolds number turbulence phenomena. The reduction of the vortex size is related to the demand of higher mass flow area as the recirculation bubbles reach their maximum length.

#### *4.2.2. Axial velocity profiles*

The high velocity region of the main stream experiences a radial growth for increasing Reynolds number, as can be clearly observed in the successive representation of the velocity fields in the symmetry plane. In order to study this effect in detail, the axial velocity profile at a distance $D$ of the front side of the plug is extracted (see dotted line for $\mathrm{Re}_h = 36$ in Fig. 5). In this section, the radial velocity component is negligible (mean values of $v_r/v_z \approx 0.003$ have been found), and the flow is not perturbed by the proximity of the plugs, neither by acceleration or expansion phenomena.

For Reynolds numbers $36 \leq \mathrm{Re}_h \leq 85$ (Fig. 7, left), the non-dimensional velocity profiles $v_z/v_{med}$ present a parabolic shape, similar to the analytic solution of the laminar flow in concentric annuli [23], which is also plotted as a reference. Nevertheless, the velocity levels are higher, due to the existence of the recirculation bubbles, that force the fluid to flow across the top (or bottom) tube section. The experimental results are contrasted with the numerical solution, with a twofold interest: the successful validation of the numerical method, and the contribution to a more detailed representation of the radial profile.

The maximum velocity value also increases with Reynolds number, especially at the lowest levels. This tendency is strictly linked to the growth of the recirculation bubble. At low Reynolds numbers, the length of the bubbles is shorter, and thus the main stream finds a wider volume to develop across the annular section. As the recirculation bubble grows, this volume diminishes and the mass flow crossing the upper cross sectional area increases.

However, for $\mathrm{Re}_h \geq 150$ (Fig. 7, right), the growth of the bubble length is less pronounced, and the maximum velocity levels remain fairly constant. It is remarkable that the velocity profiles become progressively flatter from $\mathrm{Re}_h$=164 onward, with a configuration typical for turbulent pipe flows.

## 5. Thermal-hydraulic results

### *5.1. Pressure drop*

Fig. 8 shows the evolution of Fanning friction factor with Reynolds number in the geometry under investigation. Experimental results are contrasted with the equivalent laminar friction factor for the smooth tube, also referenced to the hydraulic diameter $D_h$:

$$f_{h,s} = \frac{16}{Re_h} \frac{(D+d)\,{D_h}^3}{D^4} \tag{6}$$

This definition allows estimating the pressure drop augmentation found when a scraper is inserted in a smooth tube, for same mass flow rate:

$$\frac{\Delta p_a}{\Delta p_s} = \frac{f_h}{f_{h,s}} \frac{D^4}{(D+d)^2\,{D_h}^2} \tag{7}$$

Three regions of different nature can be inferred from the friction factor results:

- Region I ($\mathrm{Re}_h \leq 150$):

The flow is considered purely laminar, and it is characterized by a high influence of Reynolds number on friction factor. The averaged pressure drop increase in laminar regime, compared to the smooth pipe, is $\Delta p_a/\Delta p_s \approx 6$.
Next correlation can be established for Fanning friction factor:

$$f_h = 17.23{Re_h}^{-0.73}, \quad 20 \leq Re_h \leq 150 \tag{8}$$

- Region II ($150 < \mathrm{Re}_h < 300$):

The transition from laminar to turbulent flow occurs smoothly, in contrast to the pressure drop fluctuations found in smooth tubes [19]. This feature prevents from defining an accurate onset Reynolds number, and is associated to the radial velocity components induced by the insert devices [4, 16].
The onset of transition occurs at a similar Reynolds number level for which the recirculation bubbles reach their stable size (see Fig. 6). Thus, the flow configuration corresponding to flat axial velocity profiles (eg. $\mathrm{Re}_h = 265$ in Fig. 7, right), small and higher-velocity transverse vortices and long recirculation bubbles ($L/P \approx 0.3$) can be associated to low-Reynolds number transitional flow.

- Region III ($\mathrm{Re}_h \geq 300$):

Low Reynolds number turbulent flow is established. For $\mathrm{Re}_h \approx 1000$, the pressure drop augmentation with respect to the smooth pipe is $\Delta p_a/\Delta p_s \approx 40$. These huge pressure drop increases highlight the poor performance of the motionless scraper in turbulent regime. The mixing of the bulk flow induced by the insert devices enhances the resulting drag forces in turbulent flow, which play an important role in the global pressure drop characteristics. A similar behaviour was reported by Evans and Churchill [7] in the study of displaced elements in tubes, especially designed for mixing purposes.
Friction factor in region III can be correlated by

$$f_h = 1.33 {Re_h}^{-0.20}, \quad 300 \leq Re_h \leq 1500 \tag{9}$$

*5.2. Nature of the head losses*

The previous description of the flow characteristics reveals the existence of the two main phenomena yielding to an increase of pressure drop in laminar flow (Bergles and Joshi [24]): the raise of the wall shear stress, and the appearance of drag flow forces. In contrast to the smooth tube, wall shear stress augments due to the presence of the concentric rod, which increases the mean velocity in the tube, and owing to the deviation and acceleration of the mean flow, forced by the plugs which are periodically mounted on the rod. On the other hand, the plugs induce the flow separation, which is linked to the appearance of drag forces over the flow, contributing as well to the global pressure drop across the tube.
CFD simulations allow analyzing both effects, integrating the viscous forces, which are dominant in the tube and rod walls, and pressure forces, that mainly appear on the plug surfaces normal to the flow direction. To account for this analysis, a

periodic control volume extended over the scraper pitch is chosen. Two plugs are contained in this volume, thus contributing with net pressure forces over their rear and front faces. Momentum conservation over the pitch allows establishing the next forces relation:

$$\underbrace{\int_{\sigma_2}^{\sigma_1} p\vec{n}d\sigma}_{total force} = \underbrace{\int_{wall} \bar{\bar{\tau}}\vec{n}d\sigma + \int_{rod} \bar{\bar{\tau}}\vec{n}d\sigma}_{viscous force} + \underbrace{\int_{plugs} p\vec{n}d\sigma}_{pressure force} \tag{10}$$

where $\sigma_1$ and $\sigma_2$ are the annular cross-sections of the tube limiting the domain.
Fig. 9 represents the evolution of the viscous and pressure force coefficients with Reynolds number in laminar regime. As Reynolds number increases, viscous and pressure force coefficients diminish as expected. For the lowest Reynolds numbers, $15 < \mathrm{Re}_h < 50$, viscous force coefficient exceeds pressure force coefficient. However, this tendency reverses for increasing values of Reynolds number, highlighting the greater contribution of drag forces to global pressure drop. For $\mathrm{Re}_h \approx 200$, pressure forces contribute to 75% of the total forces along the tube.
The left-hand side of Eq. 10 gives the total force over the scraper pitch in terms of pressure drop. Thus, the relation between total force coefficient and the Fanning friction factor can be inferred as:

$$c_F = f_h \frac{4P}{D_h} \tag{11}$$

This result is employed to obtain the experimental value of $c_F$ from pressure drop results depicted in Fig. 8. Comparison with numerical computations is also included in Fig. 9, showing discrepancies lower than 4.5%. This good agreement serves as well as a validation of the numerical methodology.

### 5.3. Heat transfer

Heat transfer experiments were performed with propylene-glycol covering the range of Prandtl numbers Pr=150, 300 and 700. Experimental results are presented in Fig. 10 (left) in terms of $\mathrm{Nu}_h\mathrm{Pr}^{-0.5}$, for Reynolds numbers $20 \leq \mathrm{Re}_h \leq 1200$. The influence of Reynolds number on heat transfer for values $\mathrm{Re}_h > 80$ is significant, and experimental results can be correlated by:

$$Nu_h = 0.018{Re_h}^{0.98}Pr^{0.5}, \quad 80 \leq Re_h \leq 1200 \tag{12}$$

Bergles et al. [25] and Webb [26] proposed several criteria to evaluate the thermal-hydraulic performance of tube-side enhancement techniques. In this paper, criterion R3 outlined in [25] has been calculated to quantify the benefits of the insert under investigation. The performance criterion is defined as

$$\mathrm{R3} = \frac{\mathrm{Nu}_{a,h}}{\mathrm{Nu}_s}\frac{\mathrm{D}}{\mathrm{D}_h} \tag{13}$$

where $\mathrm{Nu}_{a,h}$ accounts for the heat transfer obtained with the tube insert, and $\mathrm{Nu}_s$ is the heat transfer obtained with a smooth tube for equal pumping power and heat exchange surface area. To satisfy the constraint of equal pumping power, $\mathrm{Nu}_s$ is evaluated at the equivalent smooth tube Reynolds number $\mathrm{Re}_s$, which matches

$$\mathrm{Re}_s^3 = \mathrm{Re}_{a,h}^3\frac{f_{a,h}}{f_s}\frac{\mathrm{D}^2\,(\mathrm{D}+\mathrm{d})}{\mathrm{D}_h^3} \tag{14}$$

Hausen correlations for laminar and transitional smooth pipe flows [27] were employed to calculate $\mathrm{Nu}_s$, with the geometrical characteristic $L/D \approx 85$, typical of tubular heat exchangers for food applications.

Results of R3 factor are depicted in Fig. 10 (right). Higher enhancements are observed for increasing Prandtl numbers. For the lowest smooth tube Reynolds number, $\mathrm{Re}_s \approx 60$, maximum augmentations of the order of 2 are reported. The R3 factor decreases towards a minimum value for $\mathrm{Re}_s \approx 200$, as $\mathrm{Nu}_s$ increases with laminar Reynolds number at a higher rate than reported for the scraper in the range $20 \leq \mathrm{Re}_{a,h} \leq 80$. From $\mathrm{Re}_s$=200 onward, enhancement levels increase up to maximum values R3≈5, reported for $\mathrm{Re}_s$=2300. For turbulent Reynolds numbers ($Re_s > 2300$), R3 factor decreases progressively, and enhancement levels of the order of R3≈1.5 are inferred for $\mathrm{Re}_s \approx 10^4$.

## 6. Local distributions

In the context of the present work, the numerical simulation of the flow aims at providing a fair description of the contribution of the flow structures to the pressure drop and heat transfer augmentation mechanisms. Numerical results for $\mathrm{Re}_h = 80$ are depicted in Fig. 11: the upper picture presents the non-dimensional velocity field, that reproduces faithfully the same features obtained with PIV. Below, skin friction coefficient distribution along the tube wall, and Nusselt number, are presented for the same working condition and Prandtl number Pr=300.

Maximum values of the skin friction coefficient are found in the front side of the plugs, towards the part of the tube where the bulk flow is deviated. The region of high shear stress extends towards the reduced cross-sectional region and further downstream. Progressively, the boundary layer grows along the tube wall side opposite to the plugs, yielding to a reduction of the local shear stress. Conversely, a huge region of low wall shear stress is found in the rear side of the plugs. This area is influenced by the low-velocity recirculation bubbles generated when the flow expands downstream the plugs. Similarly, the dead end close to the front side of the plugs presents also low skin friction coefficients, and only local slightly higher values are detected where the transverse vortex rolls up.

The 2D pattern depicted for the Nusselt number follows an equivalent trend: lowest values of Nusselt number ($Nu_h \approx 15$) are found downstream the plugs, in the region dominated by the recirculation bubbles. The acceleration of the flow in the reduced cross-sectional area originated by the plugs yields as well high heat transfer coefficients. This values diminish as the main stream reattaches to the tube wall. The most important difference found between the heat transfer and the wall shear stress distributions is found in the region where the main stream impacts against the plugs. Whereas low skin friction coefficients are reported in this area, high local Nusselt numbers are found ($Nu_h \approx 25$), owing to the beneficial effect of the transverse vortex for mixing and radial distribution of thermal energy.

The influence of Reynolds number in wall shear stress is depicted in Fig. 12, where the circumferentially-averaged wall shear stress is plotted along the pitchwise direction for $\mathrm{Re}_h = 30$, 80 and 120. The highest values are found for all Reynolds numbers in the region submitted to the blockage of the plugs. For increasing Reynolds numbers, the wall shear stress in this region augments, but it is also amplified in the vicinity of the plugs, especially in the front side. This means that the separation and acceleration of the flow is the origin of the higher local shear stresses, and this phenomenon is intensified as Reynolds number increases.

The results for circumferentially-averaged Nusselt number are shown in Fig. 13. For $\mathrm{Re}_h$=30, pitch-wise variations are not as pronounced as for the wall shear stress. Actually, averaged values under the plugs are similar to those found in the region of flow acceleration. However, for $\mathrm{Re}_h$=80 there exists a phenomenological change that is also reported for $\mathrm{Re}_h$=120, consisting on the higher heat transfer augmentation under the plugs and, especially, in front of them. The local enhancement in the regions affected by the blockage contribute greatly to the mean Nusselt number along the scraper pitch. This fact explains the experimental observation of higher influence of Reynolds number on heat transfer for $Re_h$>80, shown in Fig. 10 (left).

## 7. Conclusions

1. Flow pattern investigation in tubes of heat exchangers with motionless scrapers is carried out. PIV measurements are complemented with thermal-hydraulic tests and CFD computations, at low Reynolds numbers, in order to obtain a global understanding of the flow behavior.

2. A simple model of the flow pattern in the inserted tubes has been developed. Three main flow features are identified among the meandering path of the flow stream: two counter-rotating recirculation bubbles downstream the plugs, a high velocity region where the flow is strongly deviated, and a transverse vortex in the front side of the plugs.

3. The influence of Reynolds number on the flow structure is assessed. The growth of the recirculation bubbles up to their asymptotic value occurs at low Reynolds number, and affects the maximum flow local velocities and the configuration of the transverse vortex.

4. Fanning friction factor in laminar, transition and turbulent regimes is experimentally obtained. Transition occurs for $Re_h \approx 150$. In turbulent regime, the pressure drop augmentation induced by the motionless scraper is as high as 40, for $Re_h \approx 1000$. There is a clear relation between the growth of the bubbles to their maximum size and the transition to turbulence.

5. Nusselt number results for different Prandtl numbers are reported. Performance evaluation criteria demonstrates the beneficial enhancement provided by the inserts in laminar and transitional flows, with maximum values of R3≈5.

6. Numerical simulation of the flow provides an insight into the wall shear stress and heat transfer coefficient, and allows identifying the role of the local flow structures on the thermal-hydraulic performance. The deviation and high flow velocity behind the plugs yields to the higher local Nusselt number and skin friction coefficient.

## References


[1] R.L Webb, N. Kim, Principles of Enhanced Heat Transfer, second ed., Taylor and Francis, 2005.

[2] A.E. Bergles, ExHFT for fourth generation heat transfer technology, Experimental Thermal and Fluid Science 26 (2002) 335–344.

[3] R. Steinhagen, H. Müller-Steinhagen, K. Maani, Problems and costs due to heat exchanger fouling in New Zealand industries, Heat Transfer Engineering, 14 (1) (1992) 19–30.

[4] R.M. Manglik, A.E. Bergles, Heat transfer and pressure drop correlations for twisted-tape inserts in isothermal tubes, I: Laminar flows, Journal of Heat Transfer 115(4) (1993) 881–889.

[5] L. Wang, B. Sundén, Performance comparison of some tube inserts, Int. Comm. Heat Mass Transfer 29(1) (2002) 45–56.

[6] R.K. Thakur, Ch. Vial, K.D.P. Nigam, E.B. Nauman, G. Djelveh, Static mixers in the process industries - a review, Trans IChemE 81 Part A (2003) 787–826.

[7] L.B. Evans, S.W. Churchill, The effect of axial promoters on heat transfer and pressure drop inside a tube, Chem. Eng. Prog. Symp. Ser. 59 (41) (1963) 36–46.

[8] D.R. Oliver, W.J. Aldington, Heat transfer enhancement in round tubes using wire matrix turbulators: Newtonian and non-Newtonian liquids, Chem Eng Res Des 66 (1988) 555–565.

[9] F.E. Mergerlin, R.W. Murphy, A.E. Bergles, Augmentation of heat transfer in tubes by means of mesh and brush inserts, Journal of Heat Transfer 96 (1973) 145–151.

[10] P. Sivashanmugam, S. Suresh, Experimental studies on heat transfer and friction factor characteristics of laminar flow through a circular tube fitted with helical screw-tape inserts, Applied Thermal Engineering 26 (2006) 1990–1997.

[11] P. Sivashanmugam, S. Suresh, Experimental studies on heat transfer and friction factor characteristics of turbulent flow through a circular tube fitted with regularly spaced helical screw-tape inserts, Applied Thermal Engineering 27 (2007) 1311–1319.

[12] A. Tandiroglu, T. Ayhan, Energy dissipation analysis of transient heat transfer for turbulent flow in a circular tube with baffle inserts, Applied Thermal Engineering 26 (2006) 178–185.

[13] R. Kiml, A. Magda, S. Mochizuki, A. Murata, Rib-induced secondary flow effects on local circumferential heat transfer distribution inside a circular rib-roughened tube, International Journal of Heat and Mass Transfer 47 (2004) 1403–1412.

[14] J.M. Ritchie, P. Droegemueller, M.J.H. Simmons, hiTRAN® Wire Matrix Inserts in Fouling Applications, Heat Transfer Engineering 30(10-11) (2009) 876–884.

[15] A. Krueger, F. Pouponnot, Heat exchanger performance enhancement through the use of tube inserts in refineries and chemical plants - successful applications: Spirelf®, Turbotal® and Fixotal® systems, in: H. Müller-Steinhagen, M.R. Malayeri, A.P. Watkinson (Eds.), Proc. International Conference on Heat Exchanger Fouling and Cleaning VIII, Austria, 2009, pp. 399–406.

[16] A. García, J.P. Solano, P.G. Vicente, A. Viedma, Flow pattern assessment in tubes with wire coil inserts in laminar and transition regimes, International Journal of Heat and Fluid Flow 28 (2007) 516–525.

[17] M. Raffel, C. Willer, J. Kompenhans, Particle Image Velocimetry: A practical guide, first ed., Springer, 1993.

[18] F. Scarano, M.L. Reithmuller, Advances in iterative multigrid PIV image processing, Experiments in Fluids 29 (2000) 51–60.

[19] P.G. Vicente, A. García, A. Viedma, Experimental study of mixed convection and pressure drop in helically dimpled tubes for laminar and transition flow, International Journal of Heat and Mass Transfer 45 (2002) 5091–5105.

[20] R.K. Shah, A.L. London, Laminar Flow Forced Convection in Ducts, Academic Press, New York, 1978.

[21] ISO, Guide to the expression of uncertainty in measurement, first ed., ISBN 92-67-10-188-9, International Organization for Standarization, Switzerland, 1995.

[22] Y.W Chiu, J.Y. Jang, 3D numerical and experimental analysis for thermal-hydraulic characteristics of air flow inside a circular tube with different tube inserts, Applied Thermal Engineering 29 (2009) 250–258.

[23] R.B. Bird, W. E. Stewart, E.N. Lightfoot, Transport Phenomena, Wiley, New York, 1960.

[24] A.E. Bergles, S.D. Joshi, Augmentation techniques for low Reynolds number in-tube flow, in: S. Kakaç, R.K. Shah, A.E. Bergles (Eds.), Low Reynolds number flow heat exchangers, Hemisphere, Washington D.C., 1983, pp. 694–720.

[25] A.E. Bergles, A.R. Blumenkrantz, J. Taborek, Performance evaluation criteria for enhanced heat transfer surfaces, Journal of Heat Transfer 2 (1974) 239-243.

[26] R.L. Webb, Performance evaluation criteria for use of enhanced heat transfer surfaces in heat exchanger design, International Journal of Heat and Mass Transfer 24 (1981) 715–726.

[27] A.D. Kraus, Heat Exchangers, in: A. Bejan, A.D. Kraus (Eds.), Heat Transfer Handbook, John Wiley & Sons, Inc., New Jersey, 2003, pp. 829-832.

## Figure captions

Figure 1: Detail of the scraper geometry inserted in the tube

Figure 2: Experimental setup for PIV: (1) reservoir tank and filter, (2) honeycomb, (3) test section, (4) reservoir tank, (5) electric heater, (6) electromagnetic flowmeter, (7) frequency converter, (8) centrifugal pump.

Figure 3: Experimental set-up for thermal-hydraulic tests: (1) reservoir tank, (2) positive-displacement pump, (3) frequency converter, (4) control valve, (5) electrical heater, (6) Coriolis flowmeter, (7) oval-wheel flowmeter, (8, 9) inlet and outlet RTD probes, (10) differential pressure transducer, (11) 6 kVA transformer, (12) auto-transformer, (13) thin-film thermocouples, (14, 16, 19) centrifugal pumps, (15) plate heat exchanger, (17) three-way valve, (18) cooling-heating water, (20) cooling machine, (22) PID controller

Figure 4: Assessment of the mean flow structures measured in the symmetry plane (left). Streamline model of the mean flow flow structures in tubes with motionless scrapers (right)

Figure 5: PIV velocity field along the tube symmetry plane of a smooth tube with a motionless scraper inserted, $36 < \mathrm{Re}_h < 265$

Figure 6: Length of the recirculation bubble for increasing Reynolds number.

Figure 7: PIV velocity profiles for $36 < \mathrm{Re}_h < 265$. Comparison with CFD results.

Figure 8: Fanning friction factor vs. Reynolds number. Contrast with the analytical solution for smooth tube and concentric annuli.

Figure 9: Numerical computation of pressure, viscous and total force coefficients over a scraper pitch. Comparison with experimental data from pressure drop tests

Figure 10: Heat transfer results (left) and performance evaluation criteria R3 (right)

Figure 11: Numerical velocity field in the symmetry plane of the tube (up). Skin friction coefficient ($\mathrm{C}_f$) and Nusselt number ($Nu_h$) distribution along the tube wall (low) for $\mathrm{Re}_h$=80 and Pr=300.

Figure 12: Numerical results of circumferentially averaged wall shear stress distribution along the scraper pitch, for $\mathrm{Re}_h = 30$, 80 and 120

Figure 13: Numerical results of circumferentially averaged Nusselt number distribution along the scraper pitch, for $\mathrm{Re}_h = 30$, 80 and 120, and Pr=300

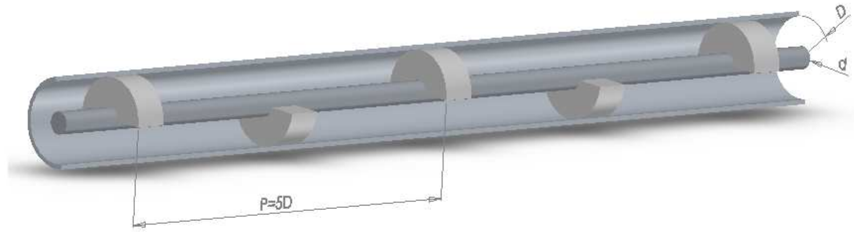
D
d
P=5D

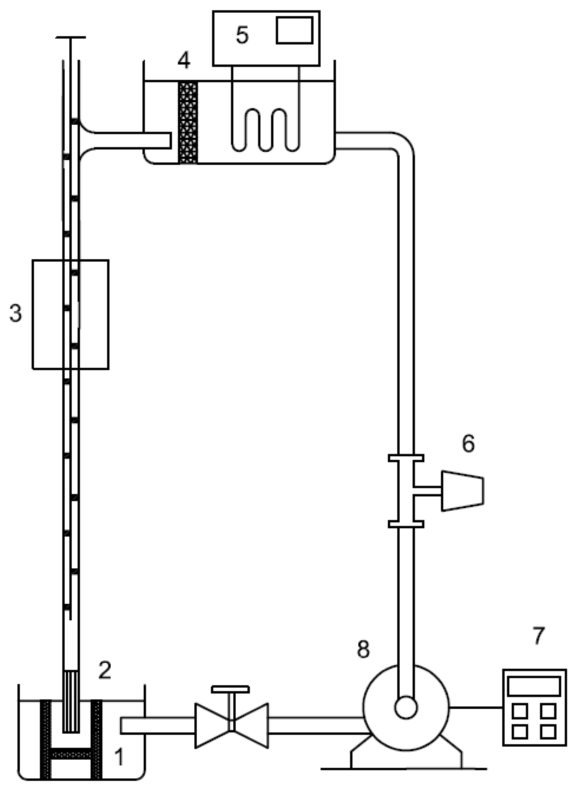
1
2
3
4
5
6
7
8

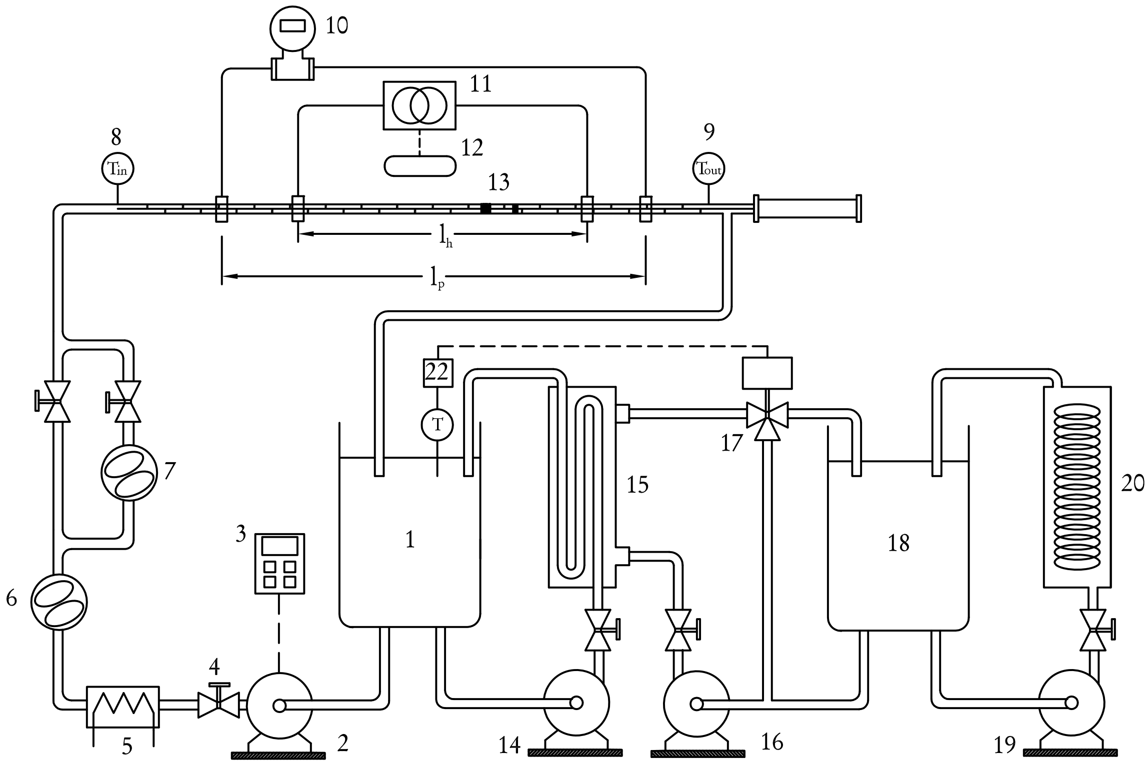
10
11
12
8
Tin
13
9
Tout
lh
lp
22
T
7
17
15
20
3
1
18
6
4
5
2
14
16
19

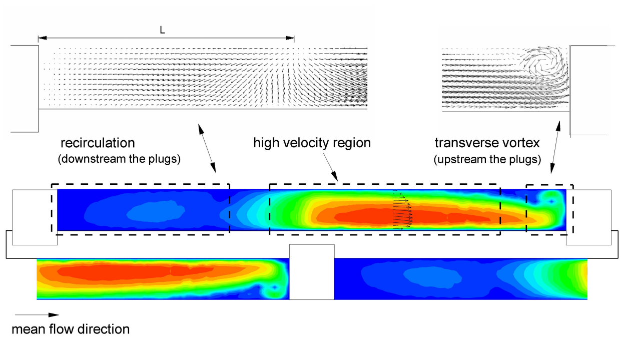
L
recirculation
(downstream the plugs)
high velocity region
transverse vortex
(upstream the plugs)
mean flow direction

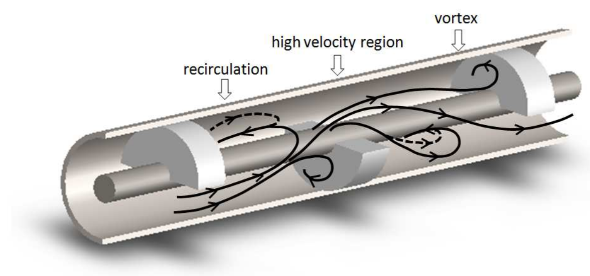
vortex
high velocity region
recirculation

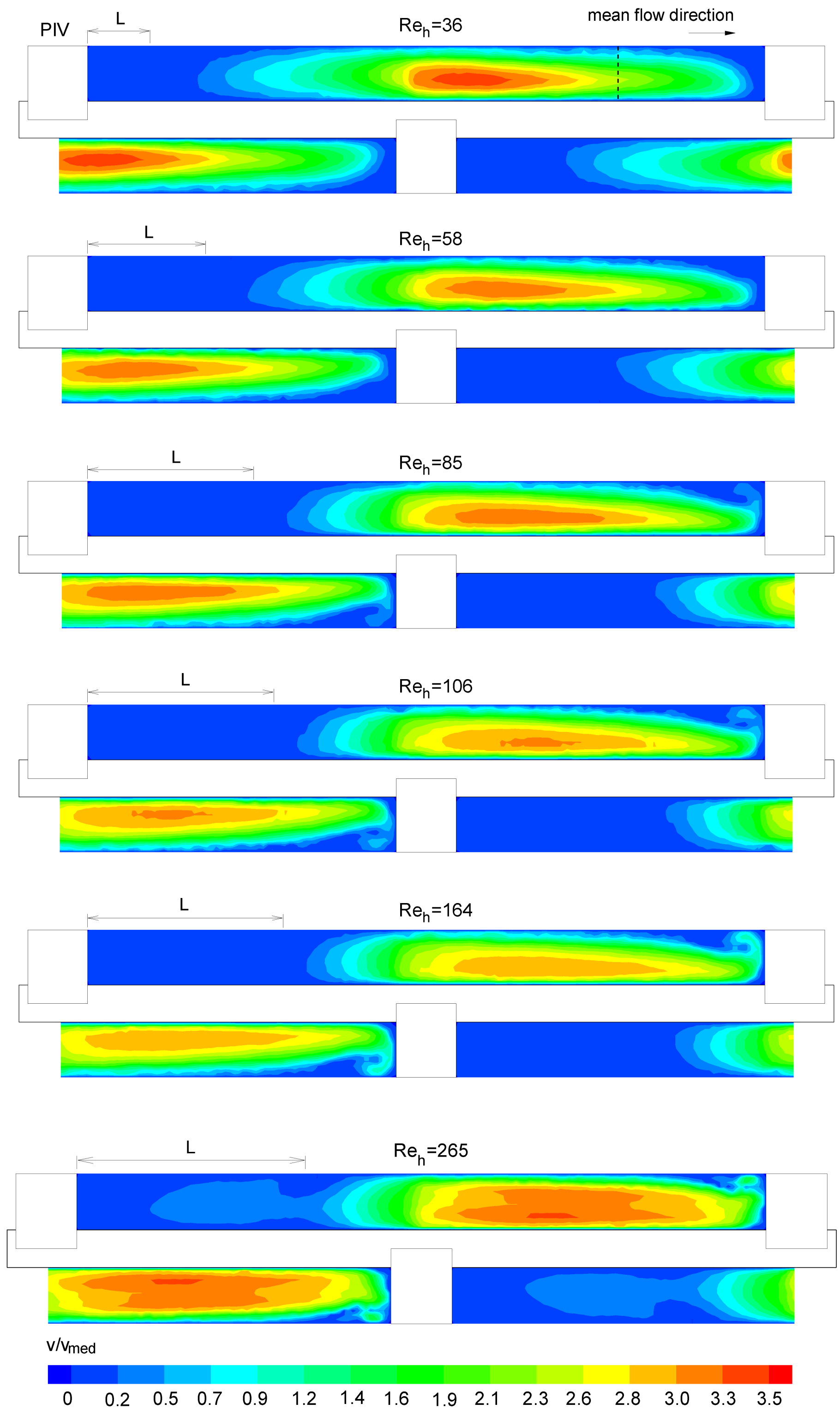
PIV
L
Re_h=36
mean flow direction
L
Re_h=58
L
Re_h=85
L
Re_h=106
L
Re_h=164
L
Re_h=265
v/v_med
0 0.2 0.5 0.7 0.9 1.2 1.4 1.6 1.9 2.1 2.3 2.6 2.8 3.0 3.3 3.5

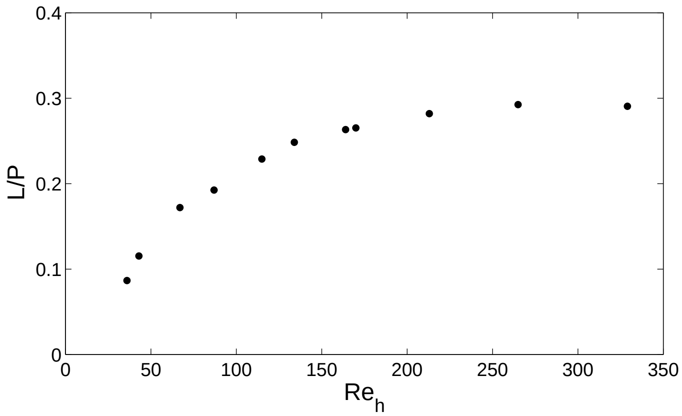

0.4
0.3
0.2
0.1
0
L/P
0
50
100
150
200
250
300
350
Re_h

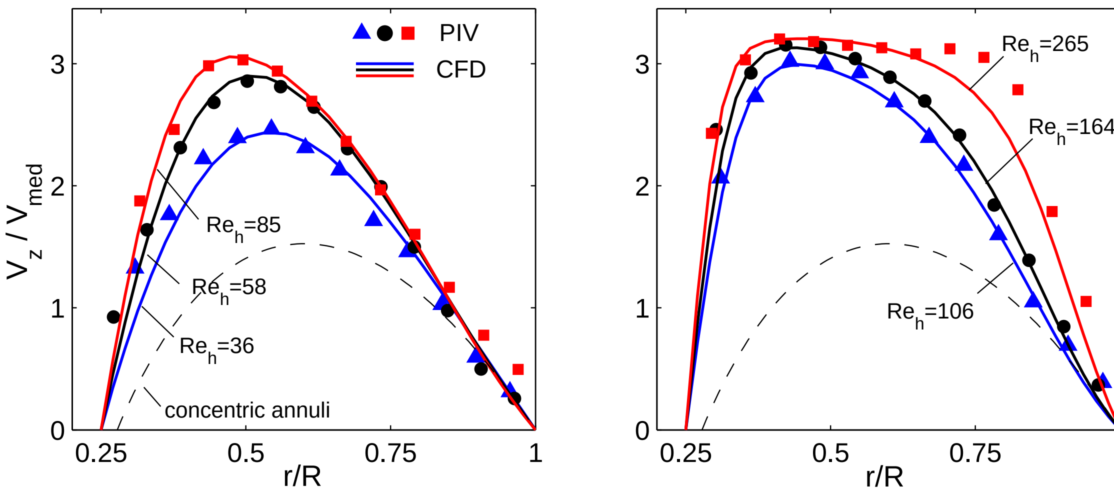
PIV
CFD
3
2
1
0
$V_z / V_{med}$
0.25
0.5
0.75
1
r/R
$Re_h$=85
$Re_h$=58
$Re_h$=36
concentric annuli
$Re_h$=265
$Re_h$=164
$Re_h$=106

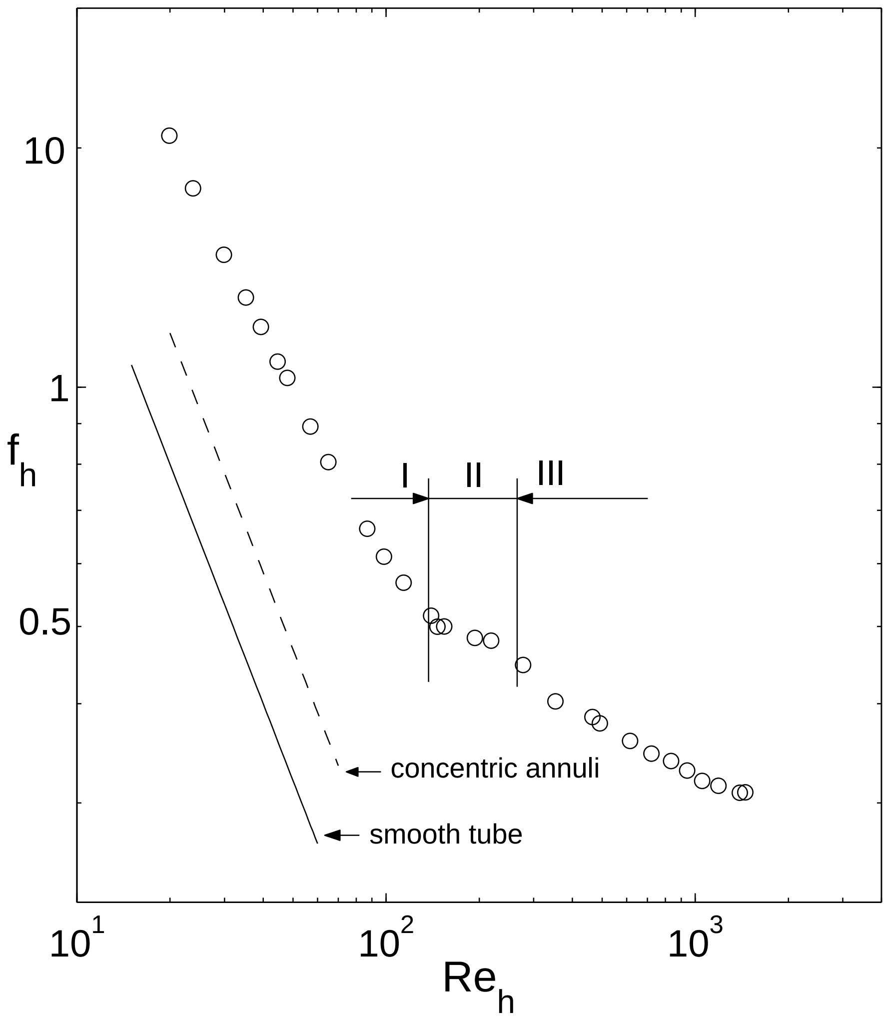
10
1
0.5
$f_h$
I
II
III
concentric annuli
smooth tube
$10^1$
$10^2$
$10^3$
$Re_h$

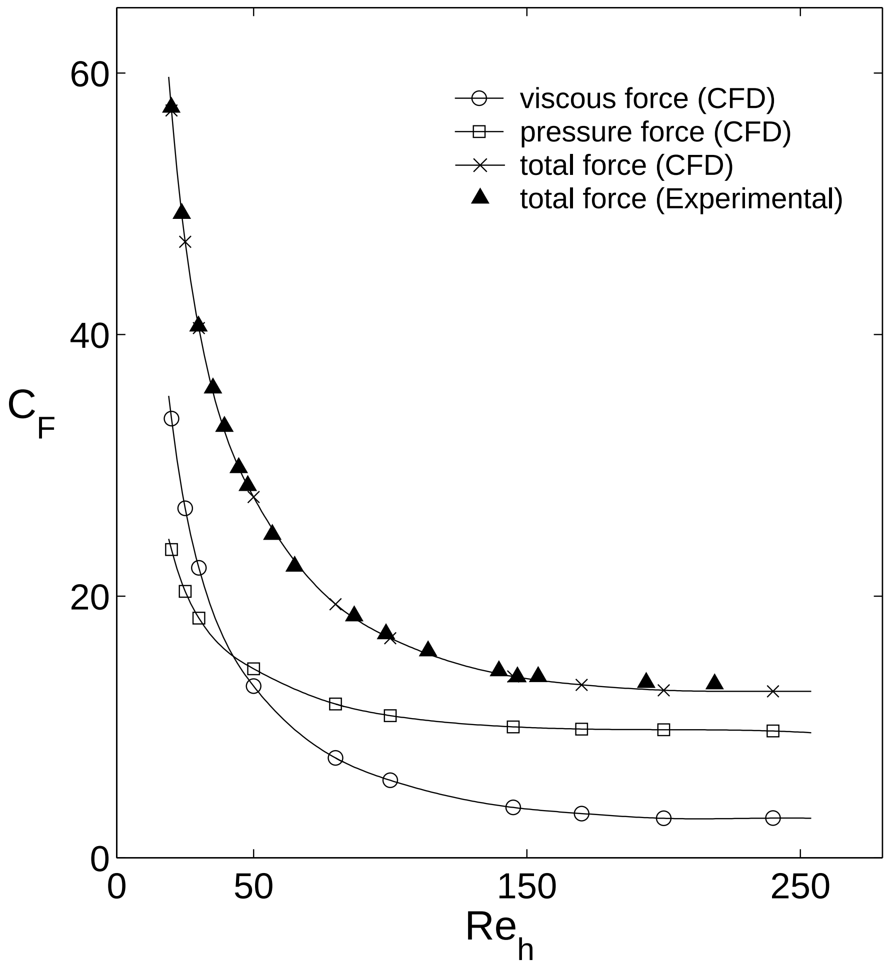

viscous force (CFD)
pressure force (CFD)
total force (CFD)
total force (Experimental)
60
40
20
0
$C_F$
0
50
150
250
$Re_h$

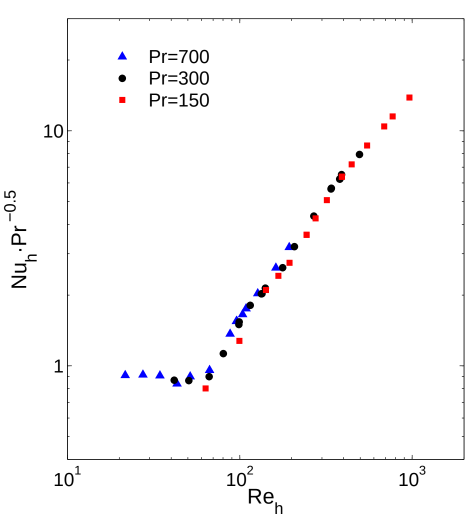
Pr=700
Pr=300
Pr=150
10
1
$10^1$
$10^2$
$10^3$
$Nu_h \cdot Pr^{-0.5}$
$Re_h$

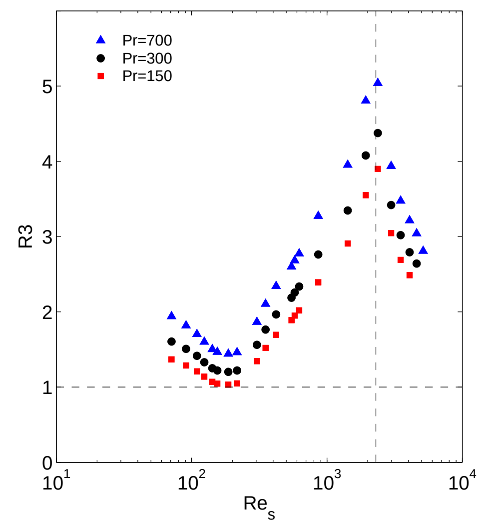
Pr=700
Pr=300
Pr=150
R3
0
1
2
3
4
5
$10^1$
$10^2$
$10^3$
$10^4$
$Re_s$

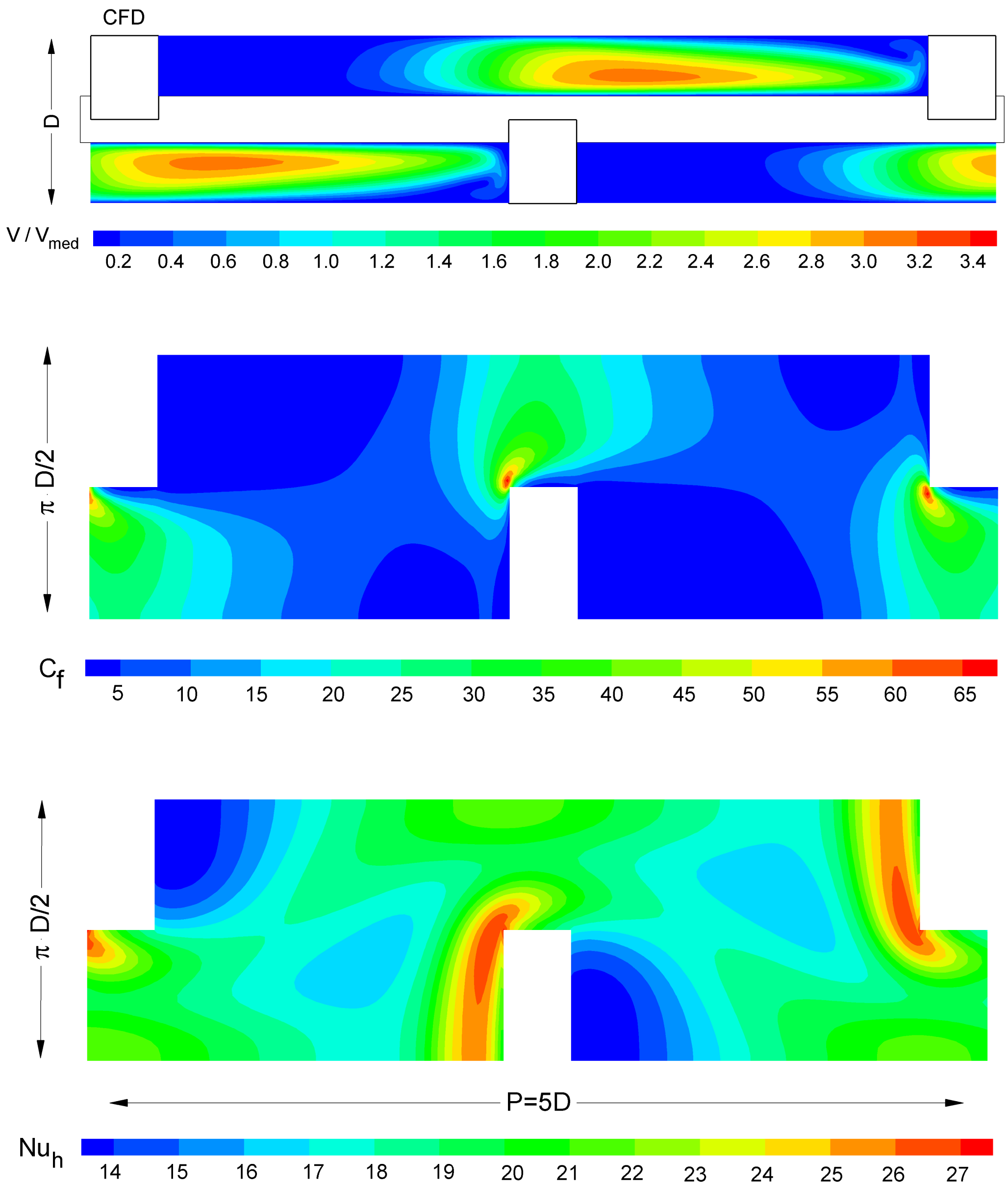
CFD
D
V / V_med
0.2 0.4 0.6 0.8 1.0 1.2 1.4 1.6 1.8 2.0 2.2 2.4 2.6 2.8 3.0 3.2 3.4
π · D/2
C_f
5 10 15 20 25 30 35 40 45 50 55 60 65
π · D/2
P=5D
Nu_h
14 15 16 17 18 19 20 21 22 23 24 25 26 27

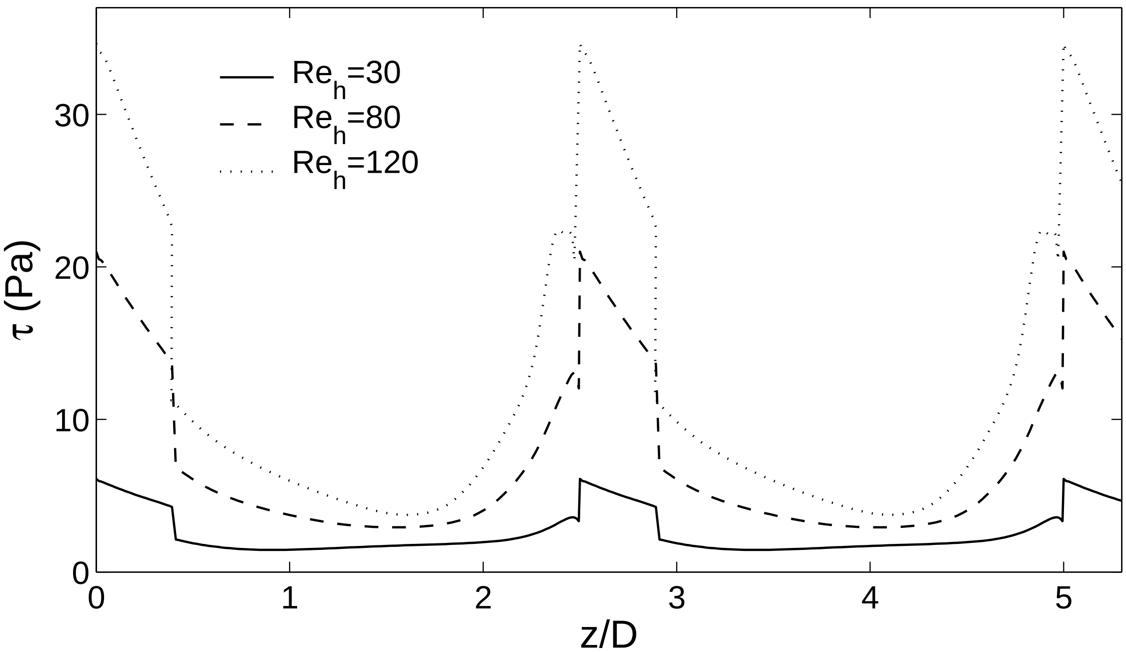

Re$_h$=30
Re$_h$=80
Re$_h$=120
τ (Pa)
z/D
0
10
20
30
0
1
2
3
4
5

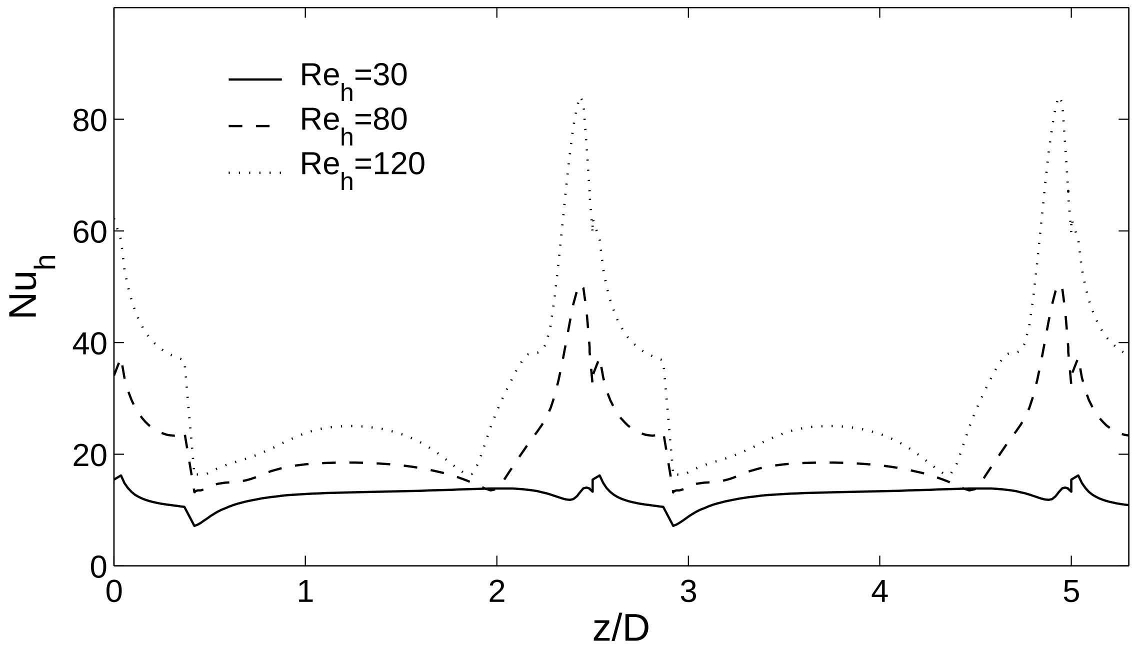

Re$_h$=30
Re$_h$=80
Re$_h$=120
Nu$_h$
z/D
0
20
40
60
80
0
1
2
3
4
5